PAPER

Numerical modelling of geodesic acoustic mode relaxation in a tokamak edge

IOP Publishing and International Atomic Energy Agency Nuclear Fusion
Nucl. Fusion **53** (2013) 063015 (10pp) doi:10.1088/0029-5515/53/6/063015

Numerical modelling of geodesic acoustic mode relaxation in a tokamak edge

M.A. Dorf[1], R.H. Cohen[1], M. Dorr[1], T. Rognlien[1], J. Hittinger[1], J. Compton[1], P. Colella[2], D. Martin[2] and P. McCorquodale[2]

[1] Lawrence Livermore National Laboratory, Livermore, CA 94550, USA
[2] Lawrence Berkeley National Laboratory, Berkeley, CA 94720, USA

Received 29 December 2012, accepted for publication 11 April 2013
Published 8 May 2013
Online at stacks.iop.org/NF/53/063015

Abstract
Geodesic acoustic modes (GAMs) are an important phenomenon in a tokamak edge plasma. They regulate turbulence in a low confinement (L-mode) regime and can play an important role in the low to high (L–H) mode transition. It is therefore of considerable importance to develop a detailed theoretical understanding of their dynamics and relaxation processes. The present work reports on the numerical modelling of collisionless GAM relaxation, including the effects of a strong radial electric field characteristic of a tokamak pedestal in a high confinement (H-mode) regime. The simulations demonstrate that the presence of a strong radial electric field enhances the GAM decay rate, and heuristic arguments elucidating this finding are provided. The numerical modelling is performed by making use of the continuum gyrokinetic code COGENT.

(Some figures may appear in colour only in the online journal)

1. Introduction

Geodesic acoustic modes (GAMs) are toroidally symmetric electrostatic wave oscillations [1]. Driven by turbulence, GAMs are universally observed in the edge of a tokamak under L-mode conditions [2–6]. They can also be excited by energetic particles, either externally injected (e.g., neutral beam injection [7]), or produced as the result of collective instabilities (e.g., tearing mode reconnection [8]). Furthermore, it has been recently proposed to employ external magnetic fields to drive GAMs either for diagnostic purposes, or to modify the turbulent transport in case a sufficiently large amplitude is achievable [9, 10]. It is therefore increasingly important to develop a detailed theoretical understanding of GAM dynamics and relaxation processes.

The original analysis of GAMs was performed by making use of an ideal electrostatic hydromagnetic model, and a non-decaying normal mode with a real frequency of $\omega_{\rm GAM} \sim V_{\rm T}/R$ was found [1]. Here, $V_{\rm T}$ is the ion thermal velocity, R is the tokamak major radius, and an order of unity electron to ion temperature ratio, $T_{\rm e}/T_{\rm i} \sim 1$, is assumed for simplicity. Taking kinetic effects into account yields the collisionless (Landau-like) mode relaxation that occurs as a result of wave-particle interactions between GAMs and the resonant passing ions [11–13]. For the case where ion finite-orbit-width (FOW) effects are neglected, the collisionless relaxation is mediated by a small subset of high-energy particles whose velocities satisfy $|{\rm v}_\parallel|/qR \sim \omega_{\rm GAM}$, or, equivalently ${\rm v}_\parallel \sim qV_{\rm T}$. Here, ${\rm v}_\parallel$ is an ion's parallel velocity, and q is the magnetic safety factor. Assuming a Maxwellian distribution for the background plasma equilibrium, it follows that the GAM relaxation rate, $\gamma_{\rm GAM}$, rapidly decays with q as $\gamma_{\rm GAM} \propto \exp(-q^2)$. The effects of ion FOW were first considered by Sugama and Watanabe [12], and a substantial enhancement of the collisionless GAM decay rate was demonstrated. However, the analysis in [12] included only the lowest-order ion FOW effects, while higher-order FOW corrections become increasingly important for large q values. A comprehensive asymptotic analysis taking into account arbitrary-order FOW effects, and therefore accurately describing GAM decay rate, including the case of $q \gg 1$, was formulated by Gao *et al* in [13].

It is important to note that the theoretical studies of collisionless GAM relaxation summarized above neglect the effects of an equilibrium radial electric field. While this assumption can be adequate for the L-mode regime, a strong radial electric field is present in the steep edge (pedestal) of a tokamak under H-mode conditions. Assuming that the characteristic length scale for variations of the plasma density is of order $L_n \sim \rho_\theta$, the poloidal ion gyroradius, it follows that a strong radial electric field of $E_r \sim V_{\rm T}B_\theta/c$ is required to sustain pedestal equilibrium [14]. Here, B_θ is the poloidal component of the magnetic field, c is the speed of light, and a subsonic pedestal is assumed. A radial electric field of this magnitude makes the $E \times B$ drift comparable to the poloidal projection of a particle's parallel velocity [14]. Therefore, the resonance condition for the interaction between GAMs and passing ions, and thus the GAM decay rate, can be modified in the steep H-mode pedestal

as compared to its L-mode counterpart. The present work reports on the numerical modelling of the collisionless GAM relaxation including the effects of a strong radial electric field, characteristic of a tokamak pedestal in a high confinement (H-mode) regime. The modelling is performed by making use of our recently developed full-f continuum gyrokinetic code COGENT [15, 16]. The simulations demonstrate that the presence of a strong radial electric field enhances the GAM decay rate, and heuristic arguments describing this finding are provided. We emphasize that the present analysis is also of considerable practical importance. In particular, it can provide insights into the use of external magnetic fields for GAM excitation in the H-mode pedestal. Also, as mentioned earlier, GAMs are intrinsically present in the edge of the tokamak, where they regulate the turbulent transport preceding the L–H transition. It is therefore of significant interest to assess evolution of the GAM relaxation rate as a steep H-mode pedestal forms, and the associated radial electric field increases.

The present paper is organized as follows: the theoretical background is summarized in section 2. Section 3 presents an independent derivation of the collisionless GAM relaxation rate for the case of a uniform background equilibrium, based on the formalism developed by Gao *et al* [13, 17]. The analytical results of section 3 are used to verify the COGENT code, and the results of the verification studies are summarized in section 4. Finally, section 5 discusses the GAM decay in the presence of a strong radial electric field, characteristic of a tokamak pedestal under H-mode conditions.

2. Theoretical model

Here, we summarize the theoretical model used to describe the collisionless relaxation of GAMs, excited about a uniform background equilibrium, i.e., uniform density and temperature profiles and a zero equilibrium electric field [12, 13]. For simplicity, we assume a magnetic geometry with concentric circular flux surfaces yielding

$$B_\varphi(r,\theta) = B_0/(1+\varepsilon\cos\theta), \tag{1a}$$

$$B_\theta(r,\theta) = \frac{\varepsilon}{q}\frac{B_0}{(1+\varepsilon\cos\theta)}, \tag{1b}$$

where B_φ and B_θ are the toroidal and poloidal components of the magnetic field, $\boldsymbol{B} = \boldsymbol{b}\cdot B$ with $\boldsymbol{b}$ denoting the unit vector along the field, r and θ are the minor radius and the poloidal angle, and $\varepsilon = r/R$ is the inverse aspect ratio. In order to find a linear GAM dispersion relation, we consider small axisymmetric perturbations of the electrostatic potential $\delta\varphi = \hat{\varphi}(\theta)\exp[\mathrm{i}k_\perp r - \mathrm{i}\omega t] + \mathrm{c.c.}$ with $e\delta\varphi/T_\mathrm{i} \ll 1$ and the ion distribution function $\delta F(r,\theta,w,\mu) = (-Z_\mathrm{i}eF_\mathrm{M}\hat{\varphi}/T_\mathrm{i} + J_0(k_\perp\rho_\mathrm{i})\hat{h})\exp[\mathrm{i}k_\perp r - \mathrm{i}\omega t] + \mathrm{c.c.}$. Here, $\hat{h}$ describes the non-adiabatic part of the ion response, $k_\perp$ and ω are the perpendicular (to the magnetic flux surface) wave vector and frequency of the GAM excitation, $w = m_\mathrm{i}\mathrm{v}^2/2$ and μ are a particle's energy and magnetic moment, m_i, Z_i, and e denote the ion mass, charge state, and the elementary charge, respectively, F_M corresponds to a uniform Maxwellian distribution, $\rho_\mathrm{i} = \mathrm{v}_\perp/\omega_\mathrm{ci}$ is the ion gyroradius with $\mathrm{v}_\perp$ denoting the perpendicular (to the magnetic field) component of a particle's velocity, $\Omega_\mathrm{i} = Z_\mathrm{i}eB/m_\mathrm{i}c$ is the ion cyclotron frequency, and $J_n(x)$ denotes the Bessel function of order n. Making use of the linearized gyrokinetic equation written in (r,θ,w,μ) variables [18] it is straightforward to obtain [13]

$$\left(\omega - \omega_\mathrm{d}\sin\theta + \mathrm{i}\omega_\mathrm{t}\frac{\partial}{\partial\theta}\right)\hat{h} = \frac{Z_\mathrm{i}eF_0}{T_\mathrm{i}}\omega J_0(k_\perp\rho)\hat{\varphi}, \tag{2}$$

where $\omega_\mathrm{t} = \mathrm{v}_\parallel/qR$ is the ion transit frequency, $\mathrm{v}_\parallel = \sqrt{(2/m_\mathrm{i})[w-\mu B(r,\theta)]}$ is the particle parallel velocity, and $\omega_\mathrm{d} = k_\perp\mathrm{v}_\mathrm{d}$ is the 'drift' frequency corresponding to $\omega_\mathrm{d} = k_\perp(2\mathrm{v}_\parallel^2 + \mathrm{v}_\perp^2)/(2\Omega_\mathrm{i}R)$ for the case of small inverse aspect ratio, i.e., $\varepsilon \ll 1$. Note that $\mathrm{v}_\parallel$ contains an explicit poloidal-angle dependence associated with the magnetic mirror force that leads to the presence of banana trajectories in equation (2). However, for the case where the bounce frequency of the banana particles, $\omega_\mathrm{B} \sim \sqrt{\varepsilon}V_\mathrm{T}/qR$, is much less that the GAM frequency, only passing particles can efficiently interact with the GAM perturbations [12, 13]. Therefore, assuming $\varepsilon \ll 1$, we can neglect the effects of the magnetic mirror force, or, equivalently, we can now consider $(r,\theta,\mathrm{v}_\parallel,\mathrm{v}_\perp)$ as independent variables in equation (2).

To determine the self-consistent evolution of the electrostatic potential perturbation, the gyrokinetic equation (equation (2)) is coupled to the quasi-neutrality condition

$$\frac{n_{0\mathrm{e}}}{T_\mathrm{e}}(\hat{\varphi} - \langle\hat{\varphi}\rangle) = -\frac{Z_\mathrm{i}}{T_\mathrm{i}}\int \mathrm{d}^3\mathrm{v}\left(Z_\mathrm{i}F_0\hat{\varphi} - \frac{T_\mathrm{i}}{e}J_0\hat{h}\right), \tag{3}$$

where a linearized adiabatic response is used for electrons, and the uniform equilibrium electron density is specified by $n_{0\mathrm{e}} = Z_\mathrm{i}n_{0\mathrm{i}}$. Here, $n_{0\mathrm{i}}$ is the equilibrium ion density. Equations (2) and (3) constitute a liner system describing the dispersion properties of the GAM excitations.

3. Dispersion relation: asymptotic analysis

Following the general approach outlined by Gao *et al* [13, 17], the asymptotic dispersion relation for the case of long wavelength GAM excitations with $k_\perp\rho_\mathrm{i} \ll 1$ is independently derived here in order to have explicit expressions for arbitrary electron to ion temperature ratio. We emphasize that along with its physical significance, such an analytical model is of great practical importance for gyrokinetic code verification studies. Representing the electrostatic potential perturbation as $\hat{\varphi}(\theta) = \sum_{l=-\infty}^{\infty}\varphi_l\exp(\mathrm{i}l\theta)$, and making use of $\exp(\mathrm{i}x\cos\theta) = \sum_{n=-\infty}^{\infty}i^nJ_n(x)\exp(\mathrm{i}n\theta)$, after some straightforward algebra it can be shown that the solution to equations (1*a*) and (1*b*) is given by [13]

$$\hat{h} = \frac{Z_\mathrm{i}eF_0}{T_\mathrm{i}}J_0(k_\perp\rho_\mathrm{i})\left[\sum_{m,n,l=-\infty}^{\infty}\varphi_l i^{m-n}\mathrm{e}^{\mathrm{i}(m-n+l)\theta}J_m\left(\frac{\omega_\mathrm{d}}{\omega_\mathrm{t}}\right)\right.$$
$$\left.\times J_n\left(\frac{\omega_\mathrm{d}}{\omega_\mathrm{t}}\right)\frac{\omega}{\omega+(n-l)\omega_\mathrm{t}}\right]. \tag{4}$$

It is instructive to note the poles at $\omega + (n-l)\omega_\mathrm{t} = 0$, or, equivalently,

$$\mathrm{v}_\parallel^\mathrm{res} = -qR\omega/(n-l) \tag{5}$$

corresponding to the resonant interactions between passing ions and collective wave-excitations. For the case of GAM excitations with $\omega = \omega_\mathrm{GAM} \sim V_\mathrm{T}/R$ it readily follows that

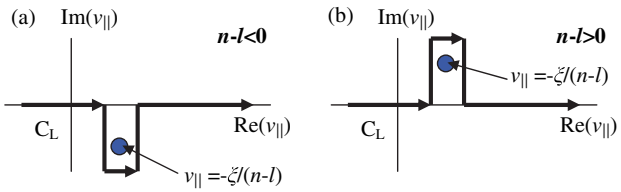

Figure 1. Integration contours used for evaluation of the integrals in equation (6). Frames (*a*) and (*b*) show Landau contours C_L corresponding to $n < l$ and $n > l$, respectively.

$v_{||}^{res} = -qV_T/(n-l)$. Further, note that the coupling between poloidal harmonics, and therefore the presence of high-order harmonics in equation (4), is provided by the term $(\omega_d \sin\theta)\hat{h}$ (in equation (2)) describing the width of the ion drift orbit. For the case of the long-wavelength excitations, $k_\perp \rho_i \ll 1$, this term is small and the spectrum of poloidal harmonics is rapidly decaying. On the other hand, for large q values, the particles that interact resonantly (in equation (5)) with low-order poloidal harmonics, i.e., $n \sim l \sim 1$, are in the high-energy tail of a Maxwellian distribution and so result in exponentially weak GAM relaxation. It is therefore increasingly important to retain higher-order poloidal harmonics as the value of q increases. The present analysis derives the asymptotic GAM dispersion relation for an arbitrary number, N, of poloidal harmonics retained.

Combining equations (3) and (4), one obtains a linear system of equations for the poloidal harmonics of the electrostatic potential perturbation

$$\left[1+\frac{T_i}{Z_i T_e}(1-\delta_{L,0})\right]\varphi_L = \int_{C_L}\frac{d^3 v e^{-v^2}}{\pi^{3/2}} J_0^2(kv_\perp) \times \sum_{n,l=-\infty}^{\infty} \varphi_l i^{-l+L} J_n(x) J_{n-l+L}(x)\frac{\xi}{\xi+(n-l)v_{||}}. \quad (6)$$

Here, $\delta_{L,0}$ is the Kronecker delta ($\delta_{n,m} = 1$ when $n = m$, and 0, otherwise) and the following normalizing variables have been introduced: $\xi = qR\omega/V_T$, $V_T = \sqrt{2T_i/m_i}$, $x = kq(2v_{||}^2 + v_\perp^2)/2v_{||}$, $v = v/V_T$, $v_{||} = v_{||}/V_T$, $v_\perp = v_\perp/V_T$, $k = k_\perp \bar{\rho}_i$, where $\bar{\rho}_i = V_T/\Omega_i$ is the thermal ion gyroradius. Note that in order to properly account for the resonant interaction between GAMs and passing ions (see equation (5)), the integration over $v_{||}$-space should be carried out along the Landau contour, C_L, as illustrated in figure 1. The GAM dispersion relation is specified by a zero determinant of the linear system in equation (6). Assuming that only N poloidal harmonics are retained in equation (6), i.e.,

$$-N \leqslant L \leqslant N, \quad -N \leqslant l \leqslant N, \quad (7)$$

we now proceed with evaluation of the matrix coefficient in equation (6).

We begin the asymptotic analysis by introducing a small parameter, $k = k_\perp \bar{\rho}_i \ll 1$, corresponding to long-wavelength GAM excitations. Excluding, for present purposes, a region of $v_{||}$ close to zero, we have $x \ll 1$, and thus $J_n(x) \sim x^{|n|}$. It now follows from equation (6) for $L \neq 0$ that $\varphi_L = k^{|L|}\varphi_0[O(1) + O(k) + O(k^2) + \cdots]$, demonstrating the rapid decay in the poloidal spectrum of the electrostatic potential perturbation. Note that retaining only N harmonics of the poloidal spectrum is equivalent to considering a block of $2N+1$ equations in system (6). The dispersion relation, can then be obtained, for instance, by substituting all φ_L's with $|L| > 0$ into the equation for the zero harmonic, i.e., equation (6) for $L = 0$. Since the terms in the right-hand side (rhs) of equation (6) for $L = 0$ are the order of $\sim k^{|n|+|n-l|}\varphi_l \sim k^{|l|}\varphi_l$, it follows that the Nth harmonic will bring a term of order $\sim k^{2N}$, and hence all other terms (in equation (6) for $L = 0$) have to be evaluated to the same accuracy. This, however, requires only $O(k^{2N-|L|})$ accuracy in the evaluation of φ_L harmonic, and therefore we only need to retain the (n, l) terms in the sums in equation (6), where n, l satisfy

$$|l| + |n| + |n-l+l| \leqslant 2N - |L|. \quad (8)$$

We now need to evaluate the rhs of equation (6), where the summation indices (n, l) are constrained by equations (7) and (8). To separate the pole contributions, it is convenient to represent the integrals in equation (6) as $\int_{C_L}\{\ldots\}d^3v = \int_{-\infty}^{\infty} dv_{||}\int_0^\infty 2\pi v_\perp dv_\perp\{\ldots\} + A_1^{l,L}$, where $\{\ldots\}$ denotes the integrand in the rhs of equation (6), and the integration in $v_{||}$ is now carried out along the real $v_{||}$-axis. The pole contributions, $A_1^L = \sum_{l=-N}^N A_1^{l,L}\varphi_l$, are determined from

$$A_1^{l,L} = -2\pi i\int_0^\infty 2v_\perp dv_\perp J_0^2(kv_\perp) \times \sum_n [1-\delta_{n,l}]\varphi_l i^{-l+L} J_n(x^*) J_{n-l+L}(x^*)\frac{\xi e^{-(\xi/(n-l))^2}}{|n-l|\sqrt{\pi}}, \quad (9)$$

where

$$x^* = kq\frac{2[\xi/(n-l)]^2 + v_\perp^2}{-2\xi/(n-l)},$$

and the multiplier $[1-\delta_{n,l}]$ is used to represent a zero pole contribution for the case where $n = l$ corresponding to the integrand $\{\ldots\}$ being a regular function. The matrix elements $A_1^{l,L}$ (in equation (9)) are assumed to be zero for the case where equation (8) does not have a solution for given values of L and l. In order to make analytical progress in evaluation of the integrals in equation (6), we now need to utilize the polynomial expansion of the Bessel functions by making use of a small parameter $x \sim k \ll 1$. However, that expansion, if performed directly inside $\{\ldots\}$, introduces terms proportional to $(1/v_{||})^p$, where $2N - |L| - |l| \geqslant p \geqslant 0$, and causes divergence of the integrals. This difficulty can be circumvented by making use of the following identity

$$\frac{1}{1+(n-l)v_{||}/\xi} \equiv \sum_{K=0}^{2N-|L|-|l|-1}(-1)^K\left[\frac{(n-l)v_{||}}{\xi}\right]^K + (-1)^{-|L|-|l|}\left[\frac{(n-l)v_{||}}{\xi}\right]^{2N-|L|-|l|}\frac{\xi}{\xi+(n-l)v_{||}}. \quad (10)$$

It is now straightforward to show that the rhs of equation (6) can be represented by $A_1^{l,L} + A_2^{l,L} + A_3^{l,L}$, where $A_{2,3}^L = \sum_{l=-N}^N A_{2,3}^{l,L}\varphi_l$, and

$$A_2^{l,L} = \int\frac{d^3 v e^{-v^2}}{\pi^{3/2}} J_0^2(kv_\perp)\sum_n (-1)^{-|l|-|L|} i^{-l+L} J_n(x) \times J_{n-l+L}(x)\left[\frac{(n-l)v_{||}}{\xi}\right]^{2N-|L|-|l|}\frac{\xi}{\xi+(n-l)v_{||}}, \quad (11)$$

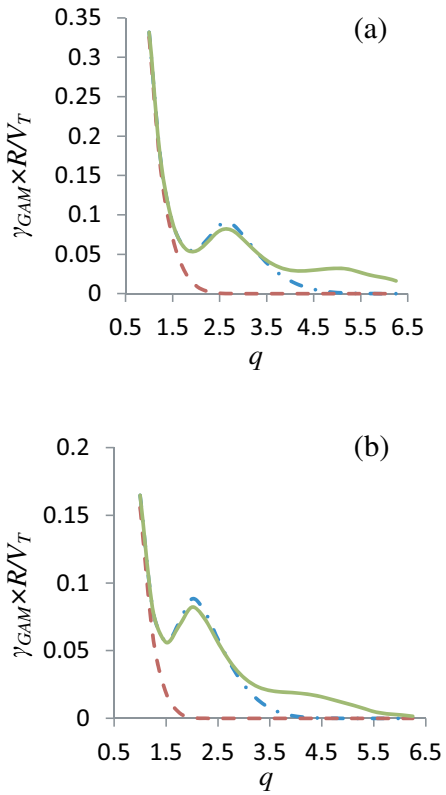

Figure 2. Illustrative numerical solution to equation (13) for the collisionless GAM relaxation rate, $\gamma_{\rm GAM}$, corresponding to $k = k_\perp \bar{\rho}_{\rm i} = 0.1375$ for the cases of (*a*) $\tau = 0.1$, and (*b*) $\tau = 1$. The number of poloidal harmonics retained in the asymptotic analysis corresponds to $N = 1$ (dashed red curves), $N = 2$ (dotted–dashed blue curves), $N = 3$ (solid green curves).

$$A_3^{l,L} = \int \frac{{\rm d}^3 v {\rm e}^{-v^2}}{\pi^{3/2}} J_0^2(kv_\perp) \sum_n \sum_{K=0}^{2N-|L|-|l|-1} (-1)^K i^{-l+L} J_n(x) \times J_{n-l+L}(x) \left[\frac{(n-l)v_{||}}{\xi}\right]^K, \quad (12)$$

where the integrals in equations (11) and (12) are taken along the real $v_{||}$-axis. The polynomial expansion of the Bessel functions can now be used for evaluating the $A_2^{l,L}$ matrix elements that involve the resonant term. At the same time, the normalized frequency, ξ, can be pulled out of the integrals in equation (12), and the $A_3^{l,L}$ elements can be directly evaluated without resorting to the Bessel function expansion. The asymptotic dispersion relation accurate through order k^{2N} is now given by

$$\mathrm{Det}[A_{l,L}(\xi)] = 0, \quad (13)$$

where $A_{l,L} = A_1^{l,L} + A_2^{l,L} + A_3^{l,L} - \delta_{l,L}[1 + \tau^{-1}(1 - \delta_{L,0})]$, and $\tau = Z_{\rm i} T_{\rm e}/T_{\rm i}$. The evaluation of $A_1^{l,L}$, $A_2^{l,L}$, and $A_3^{l,L}$ matrix elements and the practical formulation of the dispersion equation allowing for a straightforward numerical solution is provided in appendices A–D. In particular, it is noted that the sum over a limited number of n terms in equation (12) cannot provide sufficient accuracy. The n-index region is extended to include $n \in [-\infty, \infty]$ and the corresponding method for evaluation of $A_3^{l,L}$ is provided. Illustrative numerical solutions to equation (13) for the GAM decay rate are shown in figure 2. It is evident that retaining higher-order poloidal harmonics becomes increasingly important as the value of q increases. In contrast, the numerical solutions for the GAM real frequency demonstrate a weak sensitivity on the number, N, of the poloidal harmonics retained. The latter is consistent with the fact that the collective GAM oscillation is a fluid phenomenon provided by the bulk of the ion distribution function and so is insensitive to the details of the resonant interactions between GAMs and the passing ions.

Finally, we note that an analytical solution to equation (13), $\omega = \omega_{\rm GAM} - {\rm i}\gamma_{\rm GAM}$ for the GAM frequency $\omega_{\rm GAM}$, and decay rate $\gamma_{\rm GAM}$, can be obtained in the limit of $q \gg 1$ for the case where only the first poloidal harmonic is retained, i.e., $N = 1$, and is given by [13]

$$\omega^2_{{\rm GAM},N=1} = \left(\frac{7}{4} + \tau\right) \frac{V_{\rm T}^2}{R^2} \left[1 + \frac{46 + 32\tau + 8\tau^2}{(7 + 4\tau)^2 q^2}\right], \quad (14)$$

$$\gamma_{{\rm GAM},N=1} = \frac{\sqrt{\pi}}{2} \frac{V_{\rm T}}{R} \frac{(R\omega/V_{\rm T})^6}{7/4 + \tau} q^5 \exp\left[-\left(\frac{q\omega R}{V_{\rm T}}\right)^2\right]. \quad (15)$$

4. Simulation model

The dynamics of GAM excitations is studied by making use of our recently developed continuum gyrokinetic code COGENT [16–17]. The code is distinguished by the use of a fourth-order finite-volume (conservative) discretization combined with arbitrary mapped multiblock grid technology (nearly field aligned on blocks) to handle the complexity of divertor geometry with high accuracy. COGENT also includes a number of options for collision models. The present results have been obtained with the 4D (two configuration space coordinates plus two velocity space coordinates) annular closed-flux-surface version of the code (see equations (1*a*) and (1*b*)) that solves axisymmetric electrostatic multi-species gyrokinetic Boltzman–Poisson equations for the gyrocenter distribution functions $f_\alpha(\boldsymbol{R}_\alpha, {\rm v}_\parallel, \mu, t)$ and the gyroaveraged electrostatic potential $\Phi(\boldsymbol{R}_\alpha, t)$. Here, $\boldsymbol{R}_\alpha(r, \theta)$ is the gyrocenter position coordinate, ${\rm v}_\parallel$ is the parallel velocity, μ is the magnetic moment, and the corresponding kinetic equation is given by

$$\frac{\partial f_\alpha}{\partial t} + \frac{{\rm d}\boldsymbol{R}_\alpha}{{\rm d}t} \nabla f_\alpha + \frac{{\rm dv}_{\parallel\alpha}}{{\rm d}t} \frac{\partial f_\alpha}{\partial {\rm v}_\parallel} = C_\alpha[f_\alpha], \quad (16)$$

where

$$ {\rm d}\boldsymbol{R}_\alpha/{\rm d}t = \boldsymbol{V}_{\alpha,{\rm gc}} = {\rm v}_\parallel \boldsymbol{b} + \boldsymbol{V}_{\alpha,{\rm dr}}, \quad (17)$$

$$ {\rm dv}_{\parallel\alpha}/{\rm d}t = (-1/{\rm v}_{\parallel\alpha} m_\alpha) \boldsymbol{V}_{\alpha,{\rm gc}} \cdot (Z_\alpha \nabla\Phi + \mu \nabla B), \quad (18)$$

$\boldsymbol{V}_{\alpha,{\rm dr}}$ is the magnetic drift velocity composed of the $\boldsymbol{E}\times\boldsymbol{B}$ drift, curvature drift, and ∇B drift, $\boldsymbol{B} = B\boldsymbol{b}$ is the magnetic field with $\boldsymbol{b}$ denoting the unit vector along the field, and $C_\alpha[f_\alpha]$ is the collision operator. Several model collision operators have been implemented and tested in COGENT [16, 19]. These include a model parallel drag–diffusion collision operator, the Lorentz operator, and a model linearized Fokker–Planck collision operator in the form proposed by Abel *et al* in [19].

The present version of the code utilizes a long wavelength approximation, $k_\perp \bar{\rho}_\alpha \ll 1$, to represent the gyro-Poisson

equation for the electrostatic potential variations in the form,

$$\Delta^2\Phi = 4\pi e\left(n_e - \sum_\alpha Z_\alpha n_{\alpha,gc}\right) - 4\pi e^2 \sum_\alpha \frac{Z_\alpha^2}{m_\alpha \Omega_\alpha^2}\nabla_\perp \cdot (n_{\alpha,gc}\nabla_\perp \Phi). \quad (19)$$

Here, $\bar{\rho}_\alpha = V_{T\alpha}/\Omega_\alpha$ is the particle thermal gyroradius, $\Omega_\alpha = Z_\alpha eB/(m_\alpha c)$ is the cyclotron frequency, $k_\perp^{-1}$ represents the characteristic length scale for variations of the electrostatic potential, $\nabla_\perp \equiv \nabla - \boldsymbol{b}(\boldsymbol{b}\cdot\nabla)$, and $n_{\alpha,gc}$ is the gyrocenter ion density. Electrons can be modelled either kinetically or through use of a Boltzmann (in the linear limit, adiabatic) approximation, with various options for the coefficient of the Boltzmann factor. It is important to remark that the axisymmetric gyrokinetic simulation model specified by equations (16)–(19) is not accurate enough to adequately describe the slow evolution of a long wavelength neoclassical radial electric field in a quasi-stationary state [20], where the particle fluxes across the magnetic surfaces are, to order $(\rho_i/R)^2$, independent of the radial electric field and the particle transport is intrinsically ambipolar. Therefore, we restrict our studies to the analysis of a not-intrinsically-ambipolar rapid initial relaxation of the local Maxwellian distribution toward a quasi-stationary state (neoclassical quasi-equilibrium) [21]. The subsequent slow evolution of the quasi-stationary state including the evolution of the 'ambipolar' radial electric field that occurs along with the relaxation of the toroidal angular momentum on the transport time scale, $\sim\nu_c(\rho_i/R)^2$, is not considered. Here, ν_c denotes the ion–ion collision frequency. Because the toroidal angular momentum remains nearly the same during the initial not-intrinsically-ambipolar rapid relaxation, the radial electric field corresponding to the relaxed quasi-stationary state is determined as a linear function of the initial toroidal angular momentum and the pressure gradient diamagnetic flows [21].

In this section, we present the results of COGENT verification studies. We report on the modelling of the collisionless GAM relaxation for the case where the GAM perturbations are excited about a uniform equilibrium, and compare the results of the numerical simulations with the analytical results obtained in section 3. For the purposes of verification studies, the following electron Boltzman model is adopted:

$$n_e = \langle\langle n_i\rangle\rangle \frac{\exp[e\Phi/T_e]}{\langle\exp[e\Phi/T_e]\rangle}. \quad (20)$$

Here, $\langle\ \rangle$ and $\langle\langle\ \rangle\rangle$ denote a magnetic-flux-surface average and volume average (over the entire simulation domain), respectively, T_e corresponds to the electron temperature, $n_i(\boldsymbol{R}_i)$ is the gyrocenter ion density, and $Z_i = 1$ is assumed. The simulations are performed for the case of the periodic radial boundary conditions, and radially constant metric coefficients are adopted for consistency. That is, the geometry is assumed to be that with the magnetic field varying with the poloidal angle, θ, according to equations (1*a*) and (1*b*), but with a constant value of the minor radius coordinate, r, used in equations (1*a*) and (1*b*) and in metric coefficients. The initial ion density is specified by

$$n_{i0} = \bar{n}_0 + \delta_n \sin[2\pi(r - r_0)/\Delta_r], \quad (21)$$

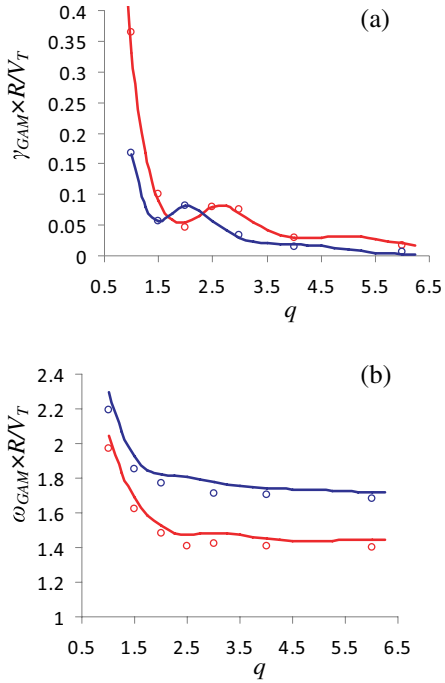

Figure 3. The collisionless relaxation of the GAM excited about a uniform equilibrium. Shown are (*a*) GAM decay rate and (*b*) frequency as a function of the magnetic safety factor, q. The results of the COGENT simulations (dots) are compared with the analytical predictions in section 3 numerically evaluated for $N = 3$. The parameters of the simulations are $Z_i = 1$, $\varepsilon = 0.2$, $k_\perp\bar{\rho}_i = 2\pi\bar{\rho}_i/\Delta_r = 0.1375$, and the ratio of the electron to ion temperature corresponds to $T_e/T_i = 1$ (blue) and $T_e/T_i = 0.1$ (red).

where $r_0 = (r_{max}+r_{min})/2$, $\Delta_r = r_{max} - r_{min}$, and r_{max} and r_{min} are the minor radius coordinates corresponding to the domain boundaries. Although the electron model in equation (20) differs from the standard neoclassical electron model [16], where $\langle\langle n_i\rangle\rangle$ in equation (20) is replaced with $\langle n_{i0}\rangle$, it is used here along with equation (19) to represent the long wavelength limit of the quasi-neutrality condition in equation (3). Indeed, assuming $n_i(r,\theta,t) = \bar{n}_0 + \tilde{n}(\theta,t)\sin(k_\perp r)$ along with $e\Phi/T_e \ll 1$, and neglecting a small 'vacuum' term in the left-hand side (lhs) of equation (19), it follows that

$$\bar{n}_0\frac{e(\Phi - \langle\Phi\rangle)}{T_e} = \tilde{n}\sin(k_\perp r) + \frac{e}{m_i\Omega_i^2}\nabla_\perp\cdot(n_i\nabla_\perp\Phi), \quad (22)$$

where the rhs of equation (22) represents a sum of the perturbed gyrodensity and polarization density corresponding to the local ion density in the rhs of equation (3) provided $k_\perp\rho_i \ll 1$.

The results of COGENT simulations are compared to the predictions of the analytical model (in section 3) for the case where the third-order resonances are retained, $N = 3$, in the asymptotic analysis (see figure 3). We note that agreement between the COGENT simulations and the theory demonstrated here is better than that reported in [22] for other gyrokinetic codes. In addition, fourth-order convergence of the numerical solution with grid resolution was demonstrated as well [17]. Figures 2 and 3 provide some illustration of sensitivity to parameters N and $\tau = Z_iT_e/T_i$; a more extensive study of parametric dependencies is outside the scope of this paper.

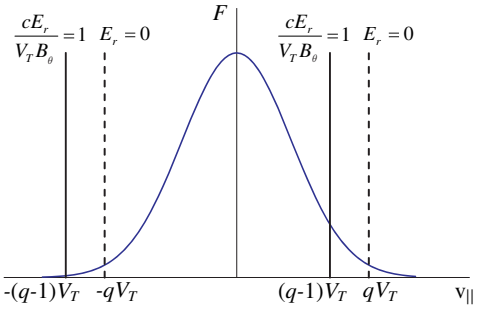

Figure 4. A schematic illustration of the primary, $N = 1$, resonances between GAMs and passing particles for the cases of $E_r = 0$ (the dashed vertical lines), and $cE_r/V_\mathrm{T}B_\theta = 1$ (the solid vertical lines).

5. Effects of a strong radial electric field

The edge of a tokamak under H-mode conditions is distinguished by the presence of steep density gradients and a strong radial electric field. Assuming a characteristic length scale for the variations of plasma density $L_n \sim \rho_\theta$, it is straightforward to show from radial force balance that the corresponding equilibrium radial electric field, E_r, is given by

$$E_r \sim V_\mathrm{T}B_\theta/c, \tag{23}$$

provided the ion toroidal (V_φ) and poloidal (V_θ) flow velocities are less than the thermal velocity, i.e., V_θ, $V_\varphi < V_\mathrm{T}$. The presence of such a strong radial electric field can substantially enhance the GAM decay rate in the H-mode tokamak pedestal. Indeed, the $E \times B$ drift becomes comparable to the poloidal projection (v_θ) of a particle's parallel velocity ($\mathrm{v}_\parallel$), and the condition of the primary resonance, i.e., $\mathrm{v}_\theta/r \sim \omega_\mathrm{GAM}$, now reads

$$|\mathrm{v}_\parallel^\mathrm{res}B_\theta/B + cE_r/B| \sim V_\mathrm{T}r/R, \tag{24}$$

where $\omega_\mathrm{GAM} \sim V_\mathrm{T}/R$ is assumed. The condition in equation (24) has two solutions for the resonant parallel velocity, which are shifted from $\pm qV_\mathrm{T}$ values due to the presence of the $E \times B$ drift (see figure 4). One solution is shifted towards the bulk of the particle distribution function and the other towards its tail. It is, however, straightforward to show (provided a safety factor, q, is not too small) that the net shift in the resonant velocities provides an increase in the number of the resonant particles, and therefore the GAM decay rate increases.

While the primary resonant interaction determines the GAM decay rate for moderate values of a safety factor, $q \sim 1$, it is the particle interaction with high-order poloidal harmonics of the GAM perturbation that provides the GAM relaxation as the value of q increases (see figure 2). Generalizing the condition in equation (24) for the case of the resonant interaction with higher-order order harmonics, it follows that the smaller (absolute) value of resonant parallel velocity is given in the presence of a radial electric field by

$$\mathrm{v}_\parallel^\mathrm{res} \sim [q/n - (c/V_\mathrm{T})|E_r/B_\theta|]V_\mathrm{T}, \tag{25}$$

where n is the harmonic order. For the case of a large safety factor, $q \gg 1$, the order, n_min, of the lowest poloidal harmonic that can resonantly interact with the bulk of the ion distribution, i.e., $\mathrm{v}_\parallel^\mathrm{res} \sim V_\mathrm{T}$, is significantly decreased in the presence of a strong electric field. For instance, $n_\mathrm{min} \sim q/2$ for $E_r = V_\mathrm{T}B_\theta/c$, in contrast to $n_\mathrm{min} \sim q$ for $E_r = 0$. Recall, that for the case of long wavelength GAM perturbations, i.e., $k_\perp\rho_\mathrm{i} \ll 1$, the excitation factor for the nth poloidal harmonic is proportional to $(k_\perp\rho_\mathrm{i})^n$, and therefore the GAM decay rate becomes significantly enhanced in the presence of a strong radial electric field for large values of q as well.

In order to test these heuristic predications we perform model simulations of the collisionless GAM decay by making use of the closed-flux-surface version of the COGENT code. In the previous section (section 4), we discussed successful verification studies for the case where the GAM perturbations are excited about a uniform plasma equilibrium with a zero equilibrium electric field. Here, we perform model simulations of the collisionless GAM decay for the case where the GAM perturbations are excited about a steep density gradient equilibrium, $L_n \sim \rho_{\mathrm{i}\theta}$, with the corresponding self-consistent equilibrium radial electric field. The temperature profile is taken to be uniform.

For these simulations we adopt the standard Boltzman electron model used in the neoclassical simulations and specified by [16]

$$n_\mathrm{e} = \langle n_{\mathrm{i}0}\rangle \frac{\exp[e\Phi/T_\mathrm{e}]}{\langle\exp[e\Phi/T_\mathrm{e}]\rangle}, \tag{26}$$

where $n_{\mathrm{i}0}$ is the initial ion gyrodensity. We assume periodic radial boundary conditions along with radially constant metric coefficients, and initialize the ion distribution function as a local Maxwellian distribution with a zero parallel flow velocity and a density profile given by

$$n_{\mathrm{i}0} = \bar{n}_0\{1 + \Delta_n \cos[2\pi(r - r_0)/\Delta_r]\}. \tag{27}$$

We note that although the bell-shaped density profile (equation (27)) assumed in the simulations does not correspond to a monotonically decaying pedestal density as in a real tokamak, the present modelling still provides important insights into assessing the influence of a strong radial electric field on the collisionless GAM relaxation. In order to simulate the initial relaxation toward a neoclassical steady state, where the self-consistent radial electric field builds up to balance the pressure gradient, we make use of a particle- and momentum-conserving Krook model [16]. Once the neoclassical quasi-stationary state is reached, the collisions are turned off adiabatically, and then a small sinusoidal perturbation in the ion distribution,

$$\delta f_\mathrm{i} = \delta_n \sin[2\pi(r - r_0)/\Delta_r]\frac{\exp(-\mathrm{v}^2/V_\mathrm{T}^2)}{\pi^{3/2}V_\mathrm{T}^3}, \tag{28}$$

is instantaneously introduced to excite the GAM perturbations. The results of the illustrative numerical simulations corresponding to the cases of a uniform density equilibrium

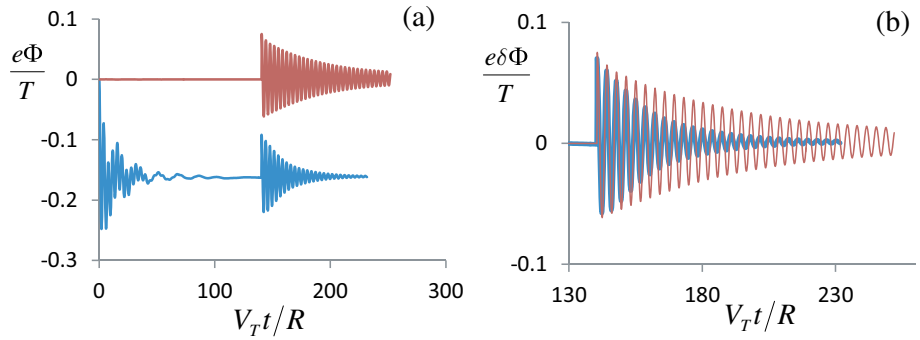

Figure 5. Collisionless GAM relaxation. (*a*) The evolution of the normalized electrostatic potential $e\Phi/T$ for the cases of a uniform density equilibrium with $\Delta_n = 0$, $E_r = 0$ (red curve) and a steep density gradient equilibrium with $\Delta_n = 0.5$, $|E_{r,\max}| \approx 0.85 \times V_T B_\theta/c$ (blue curve). Here, $|E_{r,\max}|$ corresponds to the maximum value of the self-consistent equilibrium radial electric field. (*b*) The corresponding evolution of $e\delta\Phi/T$, where $\delta\Phi(t) = \Phi(t) - \Phi_0$ is the potential perturbation about its neoclassical equilibrium value, Φ_0. The parameters of the simulations are $T = T_i = T_e$, $k_\perp \bar{\rho}_i = 2\pi\bar{\rho}_i/\Delta_r = 0.1$, $\varepsilon = 0.1$, and $q = 3$. The perturbation in equation (28) is instantaneously introduced at $V_T t/R = 140.3$.

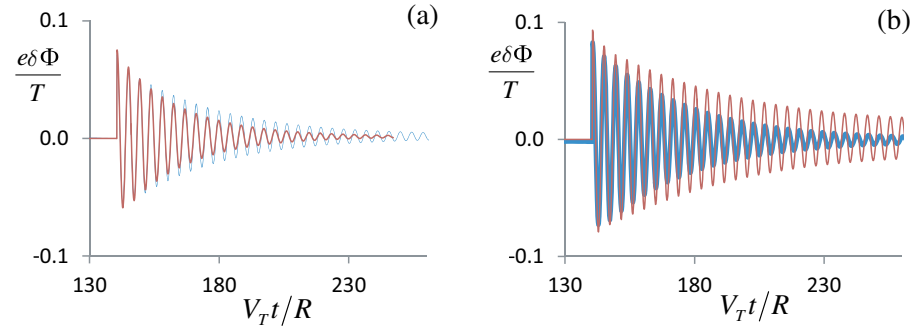

Figure 6. Collisionless GAM relaxation for the case of $T_e/T_i = 0.1$ corresponding to (*a*) $q = 3$ and (*b*) $q = 4$. Shown is the evolution of the normalized electrostatic potential perturbation $e\delta\Phi/T$ for the cases of a uniform density equilibrium with $\Delta_n = 0$, $E_r = 0$ (red curve) and a steep density gradient equilibrium with $\Delta_n = 0.5$, $|E_{r,\max}| \approx 0.85 \times V_T B_\theta/c$ (blue curve). Here, $|E_{r,\max}|$ corresponds to the maximum value of the self-consistent equilibrium radial electric field, and $\delta\Phi(t) = \Phi(t) - \Phi_0$ is the potential perturbation about its neoclassical equilibrium value, Φ_0. The parameters of the simulations are $T = T_i = 10T_e$, $k_\perp\bar{\rho}_i = 2\pi\bar{\rho}_i/\Delta_r = 0.1$ and $\varepsilon = 0.1$. The perturbation in equation (28) is instantaneously introduced at $V_T t/R = 140.3$.

($\Delta_n = 0$), and a steep density gradient equilibrium ($\Delta_n = 0.5$) are shown in figure 5(*a*) for $T_e/T_i = 1$ and $q = 3$. The results obtained here for the case of a uniform density equilibrium, i.e., $\Delta_n = 0$, have been verified to agree with the corresponding results obtained by the simulation method described in section 4. Consistent with the heuristic prediction, figure 5(*b*) shows that the presence of the strong radial electric field given in equation (23) enhances the GAM decay rate.

Additional illustrative examples corresponding to $T_e/T_i = 0.1$ are presented in figure 6. It is interesting to note that the simulations performed for the case of $q = 3$ demonstrate a slightly decreased GAM decay rate in the presence of a radial electric field (see figure 6(*a*)). This is plausibly due to the fact that the GAM relaxation in the region $2 < q < 3.5$ is primarily attributed to the resonant interaction of passing ions with the second ($n = 2$) harmonic of the GAM perturbation, for which the maximum decay rate occurs at $q \approx 3$ (see figure 2(*a*)). The presence of a strong electric field modifies the poloidal advection term in equation (2), $(v_\parallel/qR)\partial\hat{h}/\partial\theta \to (v_\parallel/qR + cE_r B_\varphi/B^2 r)\partial\hat{h}/\partial\theta$, and therefore 'effectively' corresponds to the case with no background radial electric field and a decreased value of $q_{\rm eff} \sim q[1 + (c/v_\parallel^{\rm res})|E_r/B_\theta|]^{-1}$, where $v_\parallel^{\rm res}$ is given by equation (25). For the parameters of the illustrative example in figure 6, $E_r < 0.85 \times V_T B_\theta/c$, it follows for $n = 1$ that $q_{\rm eff}^{n=1} > 2.15$, and therefore the interaction of passing ions with the first poloidal harmonic provides negligible GAM relaxation (see figure 2(*a*)) even in the presence of the radial electric field. The GAM decay is, therefore, primarily attributed to the resonant interaction with the second harmonic, which provides the strongest relaxation (in the absence of E_r) for $q \approx 3$. The presence of a background radial electric field leads to $q_{\rm eff}^{n=2} < 3$, and thus to a decreased GAM decay rate. Note that for larger values of q, the presence of a strong electric field provides enhanced GAM relaxation (see figure 6(*b*)) in accordance with the original heuristic arguments.

6. Conclusions

In the present work, we make use of the recently developed continuum gyrokinetic code COGENT [16, 17] to model the collisionless relaxation of geodesic acoustic modes (GAMs) including the effects of a strong radial electric field. Following the analysis by Gao *et al* in [13], we present an independent rigorous derivation of the collisionless GAM decay rate. The results of this analytical calculation are used to verify the COGENT code, and are found to be in excellent agreement

with the numerical results of the COGENT simulations. Based on the success of the verification studies, the code is used to model the effects of a strong radial electric field, $E_r \sim V_T B_\theta/c$ (characteristic of the H-mode tokamak pedestal), on the collisionelss GAM relaxation. Consistent with the heuristic predictions, the results of the simulations show a substantial enhancement of the GAM decay rate in the presence of a strong radial electric field.

Acknowledgment

This research was supported by the U.S. Department of Energy under contract DE-AC52-07NA27344.

Appendix A. Evaluation of $A_1^{l,L}$

We start the asymptotic evaluation of $A_1^{l,L}$ (in equation (9)) by making use of the Bessel functions power series expansion

$$J_n(x)J_{n-l+L}(x) = \sum_{m_1=\max[0,-n]}^{\infty}\sum_{m_2=\max[0,-n+l-L]}^{\infty} j_{m_1,m_2}^{n,l,L} x^{2n-l+L+2m_1+2m_2}, \quad (A.1)$$

where

$$j_{m_1,m_2}^{n,l,L} = \frac{(-1)^{m_1+m_2}}{m_1!m_2!(n+m_1)!(n-l+L+m_2)!2^{2n-l+L+2m_1+2m_2}}. \quad (A.2)$$

Now, denoting

$$P_i = \int_0^\infty 2\,\mathrm{d}v_\perp \mathrm{e}^{-v_\perp^2} J_0^2(kv_\perp) v_\perp^{2i+1} \quad (A.3)$$

and making use of the Binomial expansion

$$(x^*)^{2n-l+L+2m_1+2m_2} = (kq)^{2n-l+L+2m_1+2m_2} \times \sum_{m_3=0}^{2n-l+L+2m_1+2m_2} C_{2n-l+L+2m_1+2m_2}^{m_3} v_\perp^{2m_3} \frac{(-1)^{-l+L}}{2^{m_3}} \times \left[\frac{\xi}{(n-l)}\right]^{2n-l+L+2m_1+2m_2-2m_3} \quad (A.4)$$

it is straightforward to show

$$A_1^{l,L} = -2\sqrt{\pi} i \sum_{n,m_1,m_2,m_3} [1-\delta_{n,l}] B_{m_2,m_3}^{n,m_1} \frac{(-1)^{-l+L} P_{m_3}}{2^{m_3}} \times \left[\frac{\xi}{(n-l)}\right]^{2n-l+L+2m_1+2m_2-2m_3} \frac{\xi e^{-(\xi/(n-l))^2}}{|n-l|}, \quad (A.5)$$

where

$$B_{m_2,m_3}^{n,m_1} \equiv j_{m_1,m_2}^{n,l,L} C_{2n-l+L+2m_1+2m_2}^{m_3} i^{-l+L} (kq)^{2n-l+L+2m_1+2m_2}, \quad (A.6)$$

and C_n^k's are the binomial coefficients with

$$0 \leqslant m_3 \leqslant 2n-l+L+2m_1+2m_2. \quad (A.7)$$

Recall that to have the dispersion relation accurate through order $O(k^{2N})$, the product of Bessel functions in equation (A.1) needs to be accurate through order $O(k^{2N-|L|-|l|})$. It therefore follows that the indices m_1 and m_2 are constrained by

$$|n| \leqslant n+2m_1 \leqslant 2N - (|n-l+L| + |l| + |L|), \quad (A.8)$$

and

$$|n-l+L| \leqslant (n-l+L)+2m_2 \leqslant 2N - |l| - |L| - (n+2m_1). \quad (A.9)$$

Equations (A.8) and (A.9) can be conveniently expressed as

$$\max(0,-n) \leqslant m_1 \leqslant N - \frac{n+|n-l+L|+|l|+|L|}{2}, \quad (A.10)$$

and

$$\max[0,-(n-l+L)] \leqslant m_2 \leqslant N - \frac{(n-l+L)+|l|+|L|+(n+2m_1)}{2}. \quad (A.11)$$

Appendix B. Evaluation of $A_3^{l,L}$

First, here we note that the sum over a finite number, n, of terms in equation (12) cannot provide the required accuracy for the rhs of equation (6), i.e., $O(k^{2N-|L|})$. Indeed, for the case where $|v_{||}| < k$, the argument of the Bessel function becomes large, $x > 1$, and the asymptotic $J_n(x) \sim x^{|n|}$ is no longer valid. Further, it is straightforward to show that the contribution to the integrals in equation (12), coming from the region $|v_{||}| < k$ is of order $\mathrm{O}(k^{K+1})$ for an arbitrary Bessel function index. Therefore, the summation over n, has to be extended to include $n \in [-\infty, \infty]$. It is however still possible to evaluate $A_3^{l,L}$ by making use of the following relation [23]

$$\sum_{n=-\infty}^{\infty} n^K J_n(x) J_{n+m}(x) \equiv \sum_{j=0}^{K} b_j x^j. \quad (B.1)$$

Here, b_l's are the constant coefficients, $K \geqslant 0$, and for the special case where $K < |m|$, all b_j's are equal to zero. By making use of equation (B.1), it follows that

$$A_3^{l,L} = \sum_{K=0}^{2N-|L|-|l|-1} \sum_{j=0}^{K} (-1)^K i^{-l+L} \left(\frac{kq}{2}\right)^j a_j^{l,L} \xi^{-K} T_{K-j,j}, \quad (B.2)$$

where $a_j^{l,L}$ are determined from

$$\sum_{n=-\infty}^{\infty} (n-l)^K J_n(x) J_{n-l+L}(x) = \sum_{j=0}^{K} a_j^{l,L} x^j, \quad (B.3)$$

and the constant coefficients $T_{K-j,j}$ are given by

$$T_{a,b} = \int \frac{\mathrm{d}^3 v \mathrm{e}^{-v^2}}{\pi^{3/2}} J_0^2(kv_\perp)(2v_\parallel^2 + v_\perp^2)^b v_\parallel^a. \quad (B.4)$$

Finally, we note the although the sum over the n index has to be extended to include $n \in [-\infty, \infty]$, the sum over l including only $l \in [-N, N]$ suffices to provide the required accuracy of the rhs in equation (6), i.e., $O(k^{2N-|L|})$. Indeed, making use of $\sum_{n=-\infty}^{\infty} n^K J_n(x) J_{n+m}(x) \equiv 0$, for $K < |m|$, and recalling that $K \leqslant 2N-|L|-|l|-1$, it is straightforward to show that $A_3^{l,L} \equiv 0$ for $|l| > N$.

Appendix C. Evaluation of $A_2^{l,L}$

First, we note that the contribution to the integrals in equation (11) coming from the region $|v_{||}| < k$ is the order $O(k^{2N-|l|-|L|+1})$, and therefore can be neglected. Next, considering the region of $|v_{||}| > k$ and making use of the Bessel function expansion in equations (A.1) and (A.2), we obtain

$$A_2^{l,L} = \sum_{n,m_1,m_2,m_3} B_{m_2,m_3}^{n,m_1} P_{m_3} \frac{(-1)^{-|l|-|L|}}{2^{m_3}} \left[\frac{n-l}{\xi}\right]^{2N-|l|-|L|} Q_s, \tag{C.1}$$

where

$$s = 2N - |L| - |l| + 2n - l + L + 2m_1 + 2m_2 - 2m_3, \tag{C.2}$$

$$Q_\alpha = \int_{-\infty}^{\infty} \frac{\mathrm{d}v_{||}}{\sqrt{\pi}} \mathrm{e}^{-v_{||}^2} v_{||}^\alpha \frac{\xi}{\xi + (n-l)v_{||}}, \tag{C.3}$$

and the limits for the sum in equation (C.1) are given by equations (A.7), (A.10) and (A.11). Noticing the following recursion relation

$$\begin{aligned} Q_{\alpha+1} &= -\frac{\xi}{n-l} Q_\alpha + \frac{\xi}{n-l} \int_{-\infty}^{\infty} \frac{\mathrm{d}v_{||}}{\sqrt{\pi}} \mathrm{e}^{-v_{||}^2} v_{||}^\alpha \\ &= -\frac{\xi}{n-l} Q_\alpha + \frac{\xi}{n-l} \frac{(1+(-1)^\alpha)}{2\sqrt{\pi}} \Gamma\left(\frac{\alpha+1}{2}\right), \end{aligned} \tag{C.4}$$

we only need to evaluate Q_0. Introducing $Z(\zeta) \equiv \mathrm{i}\sqrt{\pi}\exp(-\zeta^2)[1 - \mathrm{erf}(-\mathrm{i}\zeta)]$, where $\mathrm{erf}(\zeta) \equiv (2/\sqrt{\pi}) \int_0^\zeta \exp(-x^2)\,\mathrm{d}x$, and making use of

$$Z(\zeta) = \int_{-\infty}^{\infty} \frac{\mathrm{d}t}{\sqrt{\pi}} \frac{\mathrm{e}^{-t^2}}{t-\zeta}, \tag{C.5}$$

for $\mathrm{Im}\zeta > 0$, it is straightforward to obtain

$$Q_0 = -\frac{\bar{\xi}}{|n-l|} Z\left(\frac{\bar{\xi}}{|n-l|}\right). \tag{C.6}$$

Here, we introduced $\bar{\xi} = -\xi$ (note that $\mathrm{Im}\bar{\xi} > 0$), and the recursion relation in equation (C.4) now takes the following form

$$Q_{\alpha+1} = \frac{\bar{\xi}}{n-l} Q_\alpha - \frac{\bar{\xi}}{n-l} \frac{(1+(-1)^\alpha)}{2\sqrt{\pi}} \Gamma\left(\frac{\alpha+1}{2}\right), \tag{C.7}$$

where Q_0 is given by equation (C.6). Note that for the case where $n = l$ it is straightforward to show that $A_2^{l,L} = 0$. Indeed, for that case, Q_α is a constant (see equation (C.3)), and $A_2^{l,L} \propto [n-l]^{2N-|l|+|L|} = 0$. Finally, note that the case corresponding to $|l| = |L| = N$ and $l = n$ is prohibited by the selection rule in equation (8).

Appendix D. Collected results for practical implementation

It is convenient to formulate the asymptotic dispersion relation using the variable $\bar{\xi} = -\xi$. The dispersion equation is given by

$$\mathrm{Det}[A_{l,L}(\bar{\xi})] = 0, \tag{D.1}$$

where $L, l \in [-N, N]$, and

$$A_{l,L} = A_1^{l,L} + A_2^{l,L} + A_3^{l,L} - \delta_{l,L}[1 + \tau^{-1}(1 - \delta_{L,0})]. \tag{D.2}$$

Here, $\tau = Z_\mathrm{i} T_\mathrm{e}/T_\mathrm{i}$, and the matrix elements $A_1^{l,L}(\bar{\xi})$, $A_2^{l,L}(\bar{\xi})$, and $A_3^{l,L}(\bar{\xi})$ are specified by

$$\begin{aligned} A_1^{l,L}(\bar{\xi}) &= 2\sqrt{\pi}i \sum_{n,m_1,m_2,m_3} B_{m_2,m_3}^{n,m_1} \frac{P_{m_3}}{2^{m_3}} \\ &\quad \times \left[\frac{\bar{\xi}}{(n-l)}\right]^{2n-l+L+2m_1+2m_2-2m_3} \frac{\bar{\xi} e^{-(\bar{\xi}/(n-l))^2}}{|n-l|}, \end{aligned} \tag{D.3}$$

$$A_2^{l,L}(\bar{\xi}) = \sum_{n,m_1,m_2,m_3} B_{m_2,m_3}^{n,m_1} \frac{P_{m_3}}{2^{m_3}} \left[\frac{n-l}{\bar{\xi}}\right]^{2N-|l|-|L|} Q_s, \tag{D.4}$$

$$A_3^{l,L}(\bar{\xi}) = \sum_{K=0}^{2N-|L|-|l|-1} \sum_{j=0}^{K} i^{-l+L} \left(\frac{kq}{2}\right)^j a_j^{l,L} \bar{\xi}^{-K} T_{K-j,j}, \tag{D.5}$$

where, B_{m_2,m_3}^{n,m_1}, P_i and $T_{a,b}$ are given in equations (A.6), (A.3), and (B.4) respectively, the functions Q_α are specified by the recursion relation in equations (C.6) and (C.7), the index s is given equation (C.2), the coefficients $a_j^{l,L}$ are determined from equation (B.3), and the constrains on the sum indexes n, m_1, m_2, and m_3, are given in equations (8), (A.10), (A.11), and (A.7), respectively.

References

[1] Winsor N., Johnson J.L. and Dawson J.M. 1968 *Phys. Fluids* **11** 2448
[2] Conway G.D., Angioni C., Ryter F., Sauter P., Vicente J. and the ASDEX Upgrade Team 2011 *Phys. Rev. Lett.* **106** 065001
[3] Diamond P.H., Itoh S.-I., Itoh K. and Hahm T.S. 2005 *Plasma Phys. Control. Fusion* **47** R35
[4] Conway G.D. and the ASDEX Upgrade Team 2008 *Plasma Phys. Control. Fusion* **50** 085005
[5] Hillesheim J.C., Peebles W.A., Carter T.A., Schmitz L. and Rhodes T.L. 2012 *Phys. Plasmas* **19** 022301
[6] Conway G.D., Troster C., Scott B., Hallatschek K. and the ASDEX Upgrade Team 2008 *Plasma Phys. Control. Fusion* **50** 055009
[7] Nazikian R. *et al* 2008 *Phys. Rev. Lett.* **101** 185001
[8] Chen W. *et al* 2013 *Phys. Lett.* A **377** 387
[9] Hallatschek K. and McKee G.R. 2012 *Phys. Rev. Lett.* **109** 245001
[10] Hallatschek K. and McKee G.R. 2012 Theory of external geodesic acoustic mode excitation *Proc. 24th IAEA Fusion Energy Conf. (San Diego, CA, 2012)* TH/P7-10 http://fec2012.iaea.org/contributionDisplay.py?contribId=542&sessionId=30&conId=10
[11] Lebedev V.B., Yushmanov P.N., Diamond P.H., Novakovskii S.V. and Smolyakov A.I. 1996 *Phys. Plasmas* **3** 3023
[12] Sugama H. and Watanabe T.-H. 2006 *Phys. Plasmas* **13** 012501
[13] Gao Z., Itoh K., Sanuki H. and Dong J.Q. 2008 *Phys. Plasmas* **15** 072511
[14] Catto P.J., Parra F.I., Kagan G. and Simakov A.N. 2009 *Nucl. Fusion* **49** 095026
[15] Dorf M., Cohen R.H., Dorr M., Rognlien T., Hittinger J., Compton J., Colella P., Martin D. and McCorquodale P. 2013 *Phys. Plasmas* **20** 012513

[16] Dorr M.R., Cohen R.H., Colella P., Dorf M.A., Hittinger J. and Martin D.F. 2010 Numerical simulation of phase space advection in gyrokinetic models of fusion plasmas *Proc. SciDAC 2010 Conf. (Tennessee, 2010)* http://computing.ornl.gov/workshops/scidac2010/papers/math_m_dorr.pdf
[17] Gao Z. 2010 private communications, Tsinghua University, Beijing, China
[18] Rutherford P.H. and Frieman E.A. 1968 *Phys. Fluids* **11** 569
[19] Dorf M.A. *et al* 2012 *Contrib. Plasma Phys.* **52** 518
[20] Parra F.I. and Catto P.J. 2008 *Plasma Phys. Control. Fusion* **50** 065014
[21] Hirshman S.P. 1978 *Nucl. Fusion* **18** 917
[22] Xu X.Q. *et al* 2009 *Nucl. Fusion* **49** 065023
[23] Koelink T.E. and Swarttouw R.F. 1995 *J. Approx. Theory* **81** 260